Review of Scientific Instruments

RESEARCH ARTICLE | MAY 05 2025

High definition imaging in the Mega Amp Spherical Tokamak

A. M. Patel ; N. J. Conway ; S. S. Henderson

Rev. Sci. Instrum. 96, 053501 (2025)
https://doi.org/10.1063/5.0252851

AIP Publishing

Review of Scientific Instruments ARTICLE pubs.aip.org/aip/rsi

High definition imaging in the Mega Amp Spherical Tokamak

Cite as: Rev. Sci. Instrum. 96, 053501 (2025); doi: 10.1063/5.0252851
Submitted: 12 December 2024 • Accepted: 9 April 2025 •
Published Online: 5 May 2025

A. M. Patel,[a] N. J. Conway, and S. S. Henderson

AFFILIATIONS

United Kingdom Atomic Energy Authority, Culham Campus, Abingdon, Oxfordshire OX14 3DB, United Kingdom

[a]Author to whom correspondence should be addressed: ash.patel@ukaea.uk

ABSTRACT

An absolutely calibrated, visible imaging diagnostic has been deployed on the MAST spherical tokamak. Two sets of three-color channels are defined using a combination of stacked multi-cavity interference filters, color-glass filter, and a color-pixel sensor. The system is compact with a single viewing pupil, which facilitates unambiguous comparisons of measurements in 2D. The sensor has a 12-bit dynamic range, 50 μs to 10 ms integration time (with 100–200 Hz frame rate), and a wide field of view with 640 × 480 resolution. The center-wavelength and the spectral bandpass for all colors are maintained across the field of view as they are controlled in the optical telecentric domain. The design views a complete plasma cross section, which contains passive plasma-edge and active interior emissions: one of the two neutral beam emissions, plasma-impurity charge-exchange emissions from both equator neutral beams, and two colors of bremsstrahlung.

I. INTRODUCTION

High definition visible imaging of tokamak plasmas has facilitated the measurement of plasma parameters with greater depth and confidence than by the previous generation of discrete or multi-chord systems.[1] Spatial resolutions at the plasma-equator should be at least of the order of plasma scale-lengths, such as ion Larmor radii (~1 cm at the MAST equator), contiguous and ideally over the complete plasma cross section. Such systems are useful, for example, for the study of the plasma edge region that may encompass internal transport barriers,[2] inboard-outboard asymmetries in the plasma-impurity abundance,[3] or even the neutral beam geometry parameters deep inside the plasma, such as the beam width and power deposition profile.[4]

Traditionally, intensity measurements in 2D employ an area sensor and filter combination, e.g., viewing plasma-edge radiation for shape control.[5] Intensity calibrated systems have also been used with wide field of view (FOV) optics and a multi-cavity interference filter for estimates of the equator plasma effective ion charge profile from bremsstrahlung.[6]

More sophisticated techniques with appropriately toleranced filters also measure the intensity in 2D of Doppler-shifted components of beam-neutrals.[7] These measurements are used in models that require power deposition profiles in integrated plasma modeling; these and other specialized spatial and spectral treatments of images, sometimes *in situ*, have been done.[1,8]

At the heart of the diagnostic presented here, uniquely, we avail of a large diameter telecentric optical region created by a long back-focal length, fast collection lens; here, large, high optical throughput interference filters can be used to filter the light while preserving the image quality and the spectral bandpass across the field of view (the filter diameter). The aim of the diagnostic is to measure intensities, in 2D, over the complete plasma cross-section spatial extent with six separate center wavelengths and their corresponding bandpasses that are pre-toleranced and specified. Each bandpass corresponds to the desired radiation of interest. Here, carefully specified spectral bands that pass in the red, green, and blue regions of the visible range are selected. The spatial coverage is tailored such that the complete MAST plasma, neutral beam path geometry[9,10] is encompassed. Uniquely here, the image is processed by multiple spectral bandpasses in 2D, coupled to a Bayer-pattern[11] color sensor, which is also part of the filtering process. Each bandpass is tailored to include or notch out bright line emissions. Light passes through a single pupil, which ensures that identical plasma-volume is sampled—sometimes an issue with separate high spatial resolution diagnostics—and simplifies laboratory spatial and intensity calibration as well as allowing

unambiguous comparisons between the selected emissions. Known chromatic aberrations due to the collection lens can be up to a sizable fraction of the pixel size (7.4 μm) and are included in the analysis.

II. DESIGN

Imaging a given FOV to a primary telecentric image plane, which, in turn, is imaged to an area sensor, is detailed in Ref. 6. This is developed further here with key changes in the primary optics area. The collection lens is modified in this design—it has a significant back-focal-length such that we can introduce a cube beam-splitter (see Fig. 1: we show only one of the two image channels). The large beam-splitter and refractive index of glass mean that the back focus moves further away. Multiple filters and an achromatic field lens are also located within or at the focal plane. The secondary optics area has a high-quality Fujinon lens (25 mm focal length, f/0.85) and a Bayer-pattern VGA CCD: the camera is based on a 640 × 480 Kodak inter-line CCD, 7.4 μm pixel size, and integration time 50 μs-10 ms. The sensor has a global shutter, a linear response, and 12-bit output resolution. System focusing is performed using the Fujinon lens with a large matrix-pattern object placed at the required object distance from the pupil. The pupil itself controls all solid angles to the filter normal and defines the system throughput. This f/number at the filter is maintained across the whole of the image, that is, across the whole of the FOV. The collection lens has a conically symmetric FOV and center, which is the optical axis of the instrument. Likewise, chief rays from each camera pixel center projected through the pupil are conically symmetric about the optical axis of the instrument projected to the plasma. They are optically transformed by the collection lens to a cylindrically symmetric bundle at the primary image plane (Fig. 1: image 1 and image 2)—the field lens optical center. The volume defined by the last surface of the collection lens and image 1 is telecentric. Coupling to secondary optics by the field lens serves one purpose—to converge the filtered light cone to within the aperture of the secondary optics region.

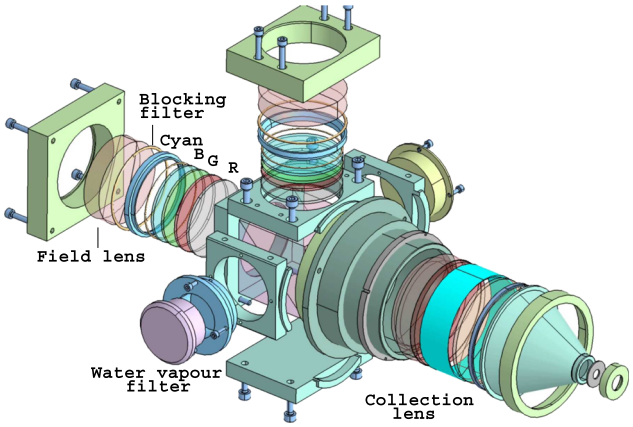

FIG. 2. Expanded view of the primary optics volume. The one is the collection lens/pupil housing. The image splitter cube is at the center of the cube structure. Also shown are the two sets of multiple filters and the achromatic field lens (shown expanded). The water vapor filter unit is also shown.

The primary optics volume consisting of filters, field lens, splitter cube, and the last surface of the collection lens is maintained in an anhydrous environment primarily for the protection of the interference filters over the long term. This is purely a precaution as some interference filters have been known by the authors to deteriorate over time due to water-vapor damage.

This system is compact (~0.7m in length) with the following parameters: image 1 is 55 mm in diameter, each filter of the stack is 2 mm thick, separated by 70 μm Teflon washers, and FOV ±25°. The solid angle subtended at image 1 is equivalent to f/10.5. Images 1 and 2 contain 5 and 4 stacked filter counts, respectively.

The mechanical arrangement with expanded detail of the collection lens and the telecentric area is shown in Fig. 2 along with the secondary optics. It is rigidly coupled within a non-ferrous opto-mechanical assembly.

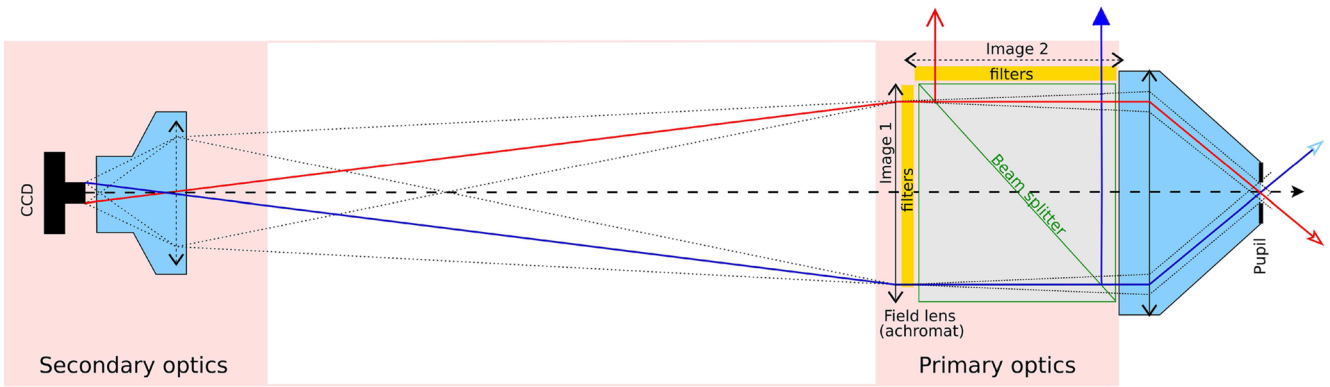

FIG. 1. Schematic diagram of the imaging system, showing FOV (red and blue), pupil/field stop. Filters are located in the yellow zone within the telecentric region of the primary optics volume. Beam-splitter cuts the light into two channels (orthogonal optics from image 2 onward not shown here), extending the primary image position further away from the last lens element of the collection lens.

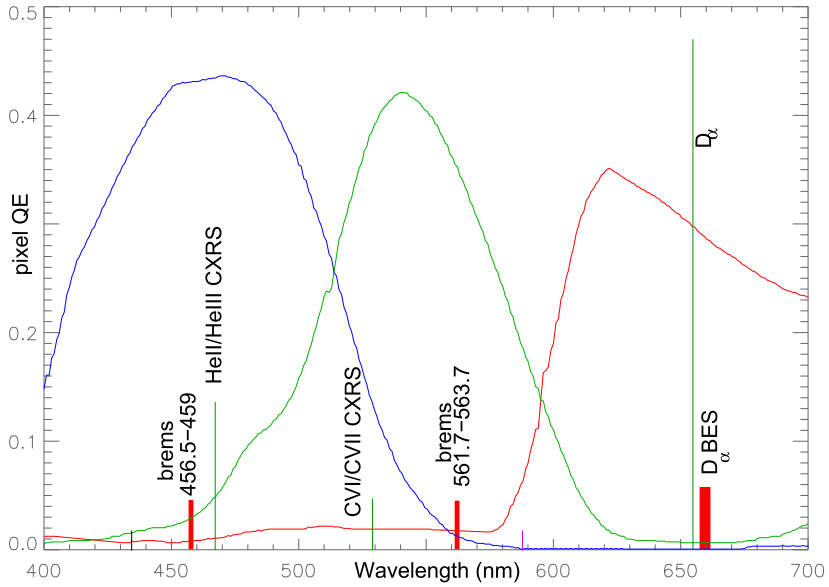

FIG. 3. Sensor pixel quantum efficiency, QE (Kodak KAI interline-transfer CCD[12]), compared with the plasma emissions studied here: D_α, He^+, and C^{5+} line radiation from image 2. A wider spectral bandwidth encompasses Doppler-shifted beam emission. Line-free green and blue bremsstrahlung are located in image 1. Of the chosen radiation, D_α dominates—a glass color filter is used, which transmits $T_{D_\alpha,He^+,C^{5+}} = [0.15,0.9,0.9]$.

III. SPECTRAL BANDPASS

A qualitative overview of the sensor pixel spectral bandpass compared with the emission intensity from the plasma edge is shown in Fig. 3. Each of the interference filter stacks contains three carefully specified interference filters. Each filter transmits near one of the peaks of the pixel response. Emissions that have been selected here are of the most interest to us from the MAST plasma. The wavelengths of interest, and their near-neighborhood, have been studied pre-design with high-resolution spectroscopy of the plasma edge in the visible range. The filters are specified with a tightly controlled center wavelength and bandpass across the whole filter area. The bandpass shape is largely defined by the filter cavity count (see Table I), also noting that the ensemble R, G, and B filters have a blue-shift due to the finite solid angle at the filter. Filter transmission across the visible range is designed as follows: R, G, and B filters have no built-in out of band blocking over the visible range as is the case during the normal manufacturing process. For example (R): single narrow bandpass at the D_α wavelength also requires broadband transmission at the other two color regions (green and blue) that contain G (C^{5+}) and B (He^+). Figure 4(a) shows the actual individual filter transmissions along with a special blocking filter designed for this stack. The pixel spectral response convolved with the filter stack is shown in Fig. 4(b)—clearly, there is undesired out of bandpass light transmission. Hence, a blocking filter is added to block these undesired residuals, which result in the overall characteristic shown in Fig. 4(c) plotted with a log axis. Here, the likely signal across the visible range from each pixel color is shown by red, green, and blue curves for a broadband source placed at the pupil. If we take the case of the blue pixel, it will pick up the majority of the signal from the B bandpass, as well as small components from the G and R bandpasses. This signal "bleeding" is due to the broad "painted pixel" QE response across the visible range, but it is stable, measurable (see Sec. IV), and unfoldable.

Table I summarizes the overall spectral characteristics measured by a high-resolution spectrometer with light sampled at the

TABLE I. Emissions under study and respective spectral bandpasses of the R, G, and B components. The filter cavity count mainly controls the overall bandpass steepness. Passive and active emissions along with bremsstrahlung are also chosen. The system characteristics are measured at the CCD lens position. "SW BE" are all Doppler-shifted beam emission components of the MAST South-West (SW) neutral beam with the passive D_α notched out.

	Image 1			Image 2		
	R	G	B	R	G	B
Passive Active	D_α	CV CVI*	HeI HeII*	 SW BE	Brem	Brem
CWL (nm) FWHM	656.11 0.81	529.51 2.36	468.86 2.60	660.00 3.92	561.90 2.08	457.23 1.98
Cavity count	2	3	3	3	3	3

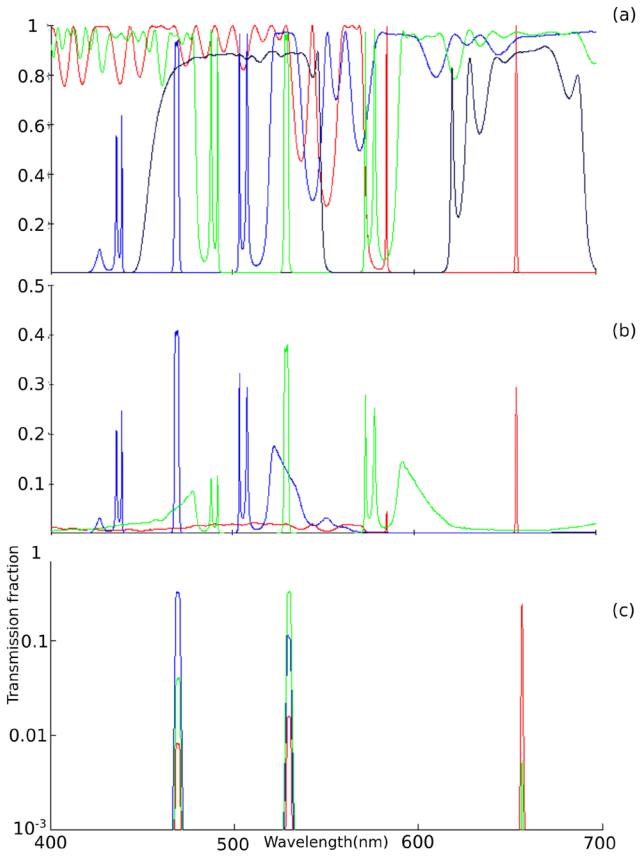

FIG. 4. Image 1 filter relative response to white-light as input: (a) Individual filter fractional R, G, and B and blocking interference filter (in black); (b) R, G, and B filters series-stacked with the CCD pixel QE (excluding the blocking filter); and (c) ensemble transmission: R, G, and B, blocker and CCD pixel QE. For a white-light source, (c) shows (qualitatively) the intensity fraction at each pass band.

secondary optics area, illuminated by a broadband source (an integrating sphere). The pixel response is broadband, and it is excluded here; it does not alter the narrow spectral bandpasses but shows the spectral properties of the primary optics system. As D_α plasma emissions are bright relative to the other two (C^{5+} and He^{+}), a "load balance" cyan color-glass filter (Andover Corporation 038FG11) is introduced such that bright D_α does not statistically overwhelm G and B signals due to signal "bleeding."

TABLE II. The **C**-matrix (see Appendix). Average values here are from the illuminated part of the VGA image. Color-additive filters of known transmission are used to measure each R, G, or B pixel and matrix element shown here.

	Image 1			Image 2		
	R	G	B	R	G	B
R	1	0.044	0.032	1	0.043	0.021 55
G	0.024	1	0.018	0.023	1	0.085
B	0.0135	0.22	1	0.012	0.026	1

In summary, the R, G, and B filter bandwidths together with blue-shifts due to its finite *f*/number illumination are such that they are narrow enough to transmit only the desired passive and active line emission (D_α, CV/CVI*, HeI/HeII*); for image 2 bandwidths as wide as possible for bremsstrahlung (G and B), the R bandpass is designed to capture Doppler-shifted D_α energy components for the range of beam operation voltages and that due to the viewing geometry but notches out the passive, bright D_α.

IV. CALIBRATION

Spatial laboratory calibrations are carried out in a straightforward manner with an illuminated matrix flat-panel that covers the complete FOV placed at a distance commensurate with the pupil–plasma–equator separation. As the whole system is circularly symmetric, only a 1D spatial calibration of the sensor pixel-row is sufficient. The focusing is achieved by using the Fujinon lens. Total system distortions are also circularly symmetric about the optical axis (of the order of 12%) and are incorporated in the analysis. Absolute sensitivity calibrations are more involved: we utilize broadband color additive filters, which, in turn, are separately calibrated for transmission at all the R, G, and B wavelengths. Each of these filters allows one bandpass and extinguishes the other two completely; they are used to measure the absolute pixel "bleeding" components, i.e., build the $\underline{C}$-matrix (see the Appendix). A calibrated integrating sphere with constant luminosity over the system FOV is used as the source. Table II summarizes the response averaged over the active part of the VGA image. Typically, the "bleed" is of the order 1–8%

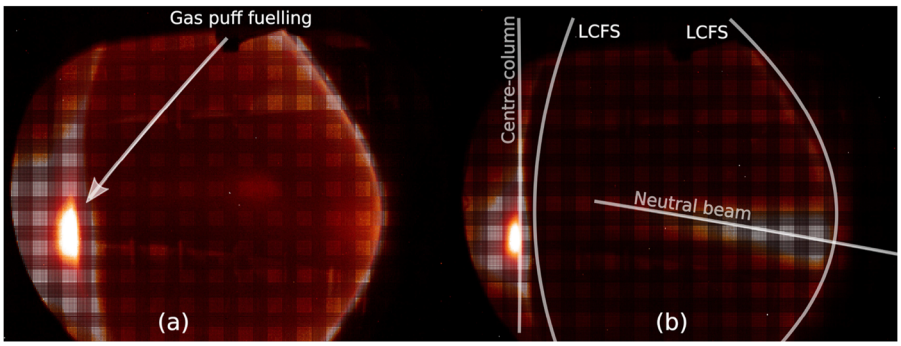

FIG. 5. One frame of raw data image from the two sensors from a MAST plasma discharge (No. 28041, integration time 190–194 ms) with a field of view that encompasses the machine axis up to and past the out-board last closed flux-surface (shown in white). The center solenoid/column and emission from one neutral beam are also shown. It should be noted that the raw data from the BGGR Bayer pattern sensor will alias with the PNG image shown here.

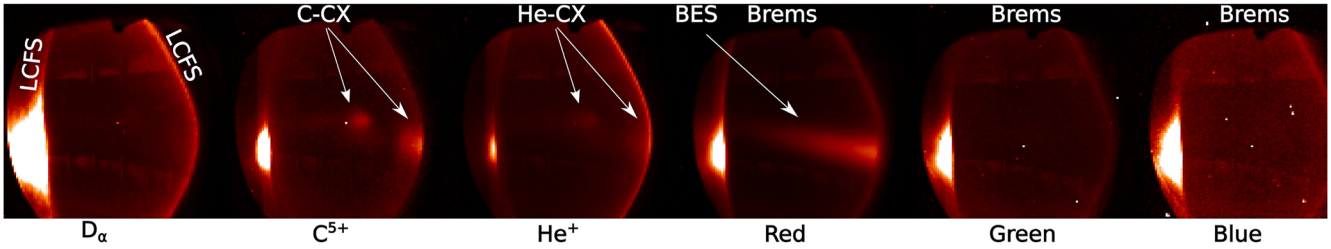

FIG. 6. Unfolded intensities into constituent radiation components from the image 1 and image 2 channels. Data here are normalized/thresholded to emphasize the chord-integrated passive (edge) and active (interior), spatially separated emissions. Placement of this diagnostic slightly above the plasma-equator allows measurements of interior charge-exchange emissions due to both neutral beams, hence two emission regions each for He-CX and C-CX.

or less. These are average values over the active region of the sensor. The procedure here measures the $\underline{C}$-matrix for each pixel and, hence, can be deconvolved for each single pixel.

V. RESULTS

A single frame of the raw data corresponding to the image 1 and image 2 channels is shown in Fig. 5, integrated over a 4 ms time period. The Bayer-pattern pixelation is apparent by eye, and some broad features, such as the neutral beam emission in Fig. 5(b), broadband emission (plasma-fueling gas puff), and the last closed flux surfaces (in-board and out-board), can be seen across the plasma cross section. Unfolding of the absolute intensities yields the three intensities per image 1 and image 2 frame—line and broad band emissions—as shown in Fig. 6. Bi-linear interpolated de-mosaicing techniques[13] have been used to obtain final VGA resolution images shown here. It should be noted that the MAST machine wall within the FOV was blackened with a graphite coating although more reflective internal plant components are seen as they were uncoated at the time. The gas puff fueling, a broadband emission, is particularly bright. D_α intensity from all Doppler-shifted energies from one beam is captured and will be of use for beam-modelling and power deposition studies. Further beam features, such as impurity charge-exchange intensity, are explored further.

Confirmation of spatial and intensity calibrations undertaken is illustrated in Fig. 7(a): here, the same passive He^+, chord-integrated measurement is compared with the equator pixel row. The separate, spatially and intensity calibrated, multi-chord spectrometer diagnostic is from another toroidal location, noting that the plasma is toroidally symmetric, which enables this comparison. Intensity cross-calibrations, such as these, are invaluable and confirm the validity of both the techniques employed here, calibrations and resilience of the two diagnostics. Figure 7(b) shows comparisons between the measured beam emission intensity and that from a model that uses experimental plasma density, temperature radial profiles, neutral beam parameters, such as voltage, current, and focusing, as well as beam-stopping, and emission atomic data. Overall, the power-deposition spatial profile form is in good agreement with NEBULA (NEutral Beam Universal Line-integrated Analysis code[14]). The absolute intensity agreement within a factor of 0.61 is under investigation but not inconsistent with other observations.[15,16] Impurity charge-exchange intensities correspond to the two neutral beams. Figures 8(a) and 8(b) illustrate the C^{5+} and He^+ charge-exchange intensity, respectively. Here, R and Z are with respect to the beam axis and vertical separation projected to the equator from the elevated position of the diagnostic/pupil. The active impurity charge-exchange peak intensity (amplitude of red ACX) for the "South" neutral beam is as shown in Figs. 8(c) and 8(d) for carbon and helium, respectively.[17]

VI. DISCUSSION

The use of custom-design multiple stacked interference filters has been demonstrated here, tailored to measure intensities in the red, green, and blue wavelength regions of the visible range. Unfolding of the signal "bleed" due to the Bayer-pattern pixel sensor is possible as the system throughput is well balanced and controlled for each color.

Here, statistics from a bright signal will not overwhelm other colors as we have taken care to balance the intensities at the sensor per image channel ("load balancing"—Sec. III). The image 1 and 2

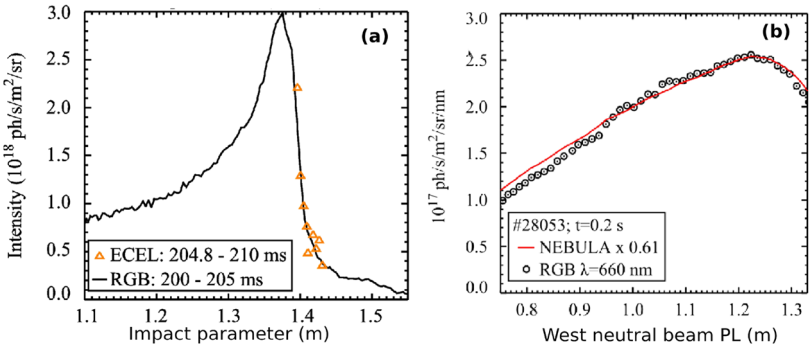

FIG. 7. (a) Passive He^+ intensity compared with an independent separate multi-chord, chord-integrating diagnostic measurement (No. 28208 204.8–210 ms, 205–210 ms, respectively) showing good agreement in intensity and spatially and (b) beam emission intensity (all energy components) compared with model calculations as a function of the beam travel.

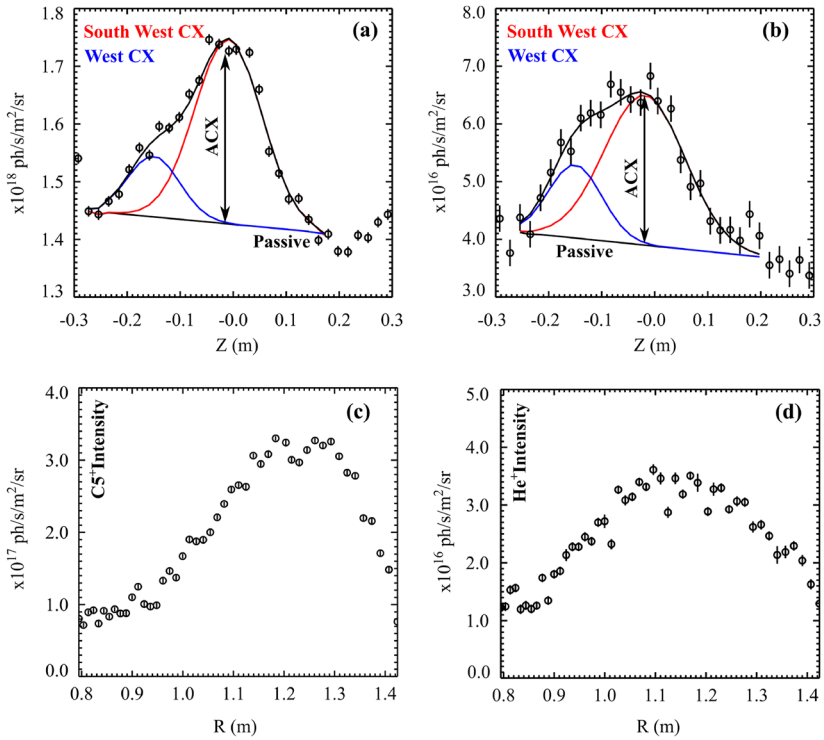

FIG. 8. Charge-exchange intensities from the two neutral beams within the FOV of the diagnostic: (a) and (b) are in the machine vertical plane for carbon and helium, respectively, and (c) and (d) show fitted amplitudes in the machine horizontal plane, i.e., along the beam travel path. ACX (in red) is the active charge-exchange "South" neutral beam intensity, while the blue curve corresponds to the "South-West" neutral beam.

channels are, in addition, separated/selected as "bright" and "dim" image channels: at typical signal levels, we expect $\lesssim$1.6% errors due to variances and error propagation, as outlined in the last section of the Appendix. In addition, as "painted-pixel" sensors are used here, this means that demosaicing techniques have to be used to interpolate the "missing" colors/pixels. In contrast to the sensor used here, multi-CCD sensors (such as 3CCD) with flat broadband spectral response over the red, green, and blue are a logical next step. They also have a much higher overall QE and can have minimal "bleeding" issues. It will benefit not only the effective dynamic range of each color but also the statistical impact of very bright or unbalanced color components. In theory, a multi-CCD combination upward of four colors is possible: The Appendix is still applicable for four or more colors.

The diagnostic here measures intensities in 2D from one pupil and many emissions that would take several separate monochromatic systems on MAST, saving on port access, etc. The single pupil enables unambiguous spatial cross-checking. In principle, the technique employed here is well suited for other research domains where known and/or tight spectral control is required and can be built or designed in research domains, such as passive/active microscopy, astronomy, and agriculture.

ACKNOWLEDGMENTS

The authors would like to thank P.G. Carolan for technical contributions. This work was funded by the EPSRC Energy Programme (Grant No. EP/W006839/1).

AUTHOR DECLARATIONS

Conflict of Interest

The authors have no conflicts to disclose.

Author Contributions

A. M. Patel: Conceptualization (equal); Data curation (equal); Formal analysis (equal); Funding acquisition (equal); Investigation (equal); Methodology (equal); Project administration (equal); Resources (equal); Software (equal); Supervision (equal); Validation (equal); Visualization (equal); Writing – original draft (equal); Writing – review & editing (equal). **N. J. Conway**: Conceptualization (equal); Data curation (supporting); Formal analysis (supporting); Funding acquisition (supporting); Investigation (supporting); Methodology (equal); Project administration (supporting); Resources (supporting); Software (supporting); Supervision (supporting); Validation (supporting); Visualization (supporting); Writing – original draft (supporting); Writing – review & editing (supporting). **S. S. Henderson**: Formal analysis (equal).

DATA AVAILABILITY

To obtain further information on the data and models underlying this paper, please contact PublicationsManager@ukaea.uk.

APPENDIX: UNFOLDING SIGNALS FROM A TRIPLE WAVELENGTH FILTERED 2D RGB CAMERA

1. Introduction

In an RGB CCD camera, there are essentially three channels at each point broadly covering the red, green, and blue spectral regions. In reality, each region of 3 (or 4) CCD elements has prefiltering of the light (or QE) so that there is a superpixel of 3 (or 4) pixels. In a total matrix of pixels, three almost identical images are captured at three spectral regions. The idea is to have an additional narrow bandwidth filter, which selects three wavelengths at discrete locations (i.e., spectral lines) within these broad bandwidths. However, the broadband profiles overlap considerably so that, in general, flux at a particular wavelength will have spill over into the other two channels, producing three signals. In principle, this can be unfolded. Here, to keep the calibration process clear, the mathematics is very explicit for each step in the process, from details of absolute calibration to propagation of errors.

2. Single pixel calibration

A broadband (calibrated) lamp will provide a continuous spectrum of brightness $S(\lambda)$ ($\mathrm{ET}^{-1}\ \mathrm{L}^{-3}\ \Omega^{-1}$), where E, T, and Ω are energy, time, and solid angle units and L^{-3} is composed of L^{-2} for area and L^{-1} for wavelength. The brightness transmitted through a filter with a transmission profile $f(\lambda)$ is given by

$$\int f(\lambda)S(\lambda)d\lambda. \tag{A1}$$

It is more convenient to represent the filter transmission as $f(\lambda) = c_m\phi_m(\lambda)$, where c_m is the peak transmission. In the case of a filter that transmits over one or more narrow spectral regions, this may be approximated to

$$\sum_{m=1}^{n} \int f_m(\lambda)d\lambda S(\lambda_m) = \sum_{m=1}^{n} c_m \int \phi_m(\lambda)d\lambda S(\lambda_m) \equiv \sum_{m=1}^{n} i_m, \tag{A2}$$

where λ_m is the transmission weighted central wavelength of the mth bandpass region in a total of n regions. We can replace $\int \phi_m(\lambda)d\lambda \equiv w_m$ as it is the equivalent of a bandwidth. Hence, we get $i_m = c_m w_m S_m$. However, it is the source brightness that we need to retain as the calibration source from an integrating sphere represents the same geometry presented by the plasma as seen by the *complete* detection system, including filters, losses, and QE. Selecting central wavelengths separately at a time, a triple filter (i.e., $n = 3$) will produce signals in a unit time in each of the three RGB channels, i.e.,

CWL		Brightness ($\mathrm{EL}^{-2}\ \Omega^{-1}$)		Signals i_1	i_2	i_3	Channel
λ_1		i_1		S_{1R}	S_{2R}	S_{3R}	R
λ_2	*	i_2	⇒	S_{1G}	S_{2G}	S_{3G}	G
λ_3		i_3		S_{1B}	S_{2B}	S_{3B}	B

On normalization (i.e., calibration),

It is more convenient from the mathematics to reassign the S_* subscripts so that

CWL	Intensity ($\mathrm{EL}^{-2}\ \Omega^{-1}$)		Calibrated signals			Channel
λ_1	1		S_{1R}/i_1	S_{1R}/i_2	S_{1R}/i_3	R
λ_2	1	⇒	S_{2G}/i_1	S_{2G}/i_2	S_{2G}/i_3	G
λ_3	1		S_{3B}/i_1	S_{3B}/i_2	S_{3B}/i_3	B

CWL	Intensity ($\mathrm{EL}^{-2}\Omega^{-1}$)		Calibrated signals			Channel
λ_1	1		S_{11}/i_1	S_{12}/i_2	S_{13}/i_3	R
λ_2	1	⇒	S_{21}/i_1	S_{22}/i_2	S_{23}/i_3	G
λ_3	1		S_{31}/i_1	S_{32}/i_2	S_{33}/i_3	B

or

CWL	Intensity ($\mathrm{EL}^{-2}\Omega^{-1}$)		Calibrated signals	Channel
λ_1	1		$C_{11}C_{12}C_{13}$	R
λ_2	1	⇒	$C_{21}C_{22}C_{23}$	G
λ_3	1		$C_{31}C_{32}C_{33}$	B

We define the matrix

$$\underline{C} \equiv \begin{pmatrix} C_{11} & C_{12} & C_{13} \\ C_{21} & C_{22} & C_{23} \\ C_{31} & C_{32} & C_{33} \end{pmatrix},$$

which summarizes the calibration above.

3. Responses to arbitrary illumination from three discrete spectral lines

When the widths of the spectral lines of interest are small compared with the filter bandwidths (and the lines are aligned with the filter peaks), the transmitted intensity at λ_k will be $t_k \equiv I_k c_k \phi_k(\lambda_k)$, where I_k is the source brightness for the kth line. Intensities at the discrete wavelengths, ${}_d\lambda_{1,2,3}$ of $I_{1,2,3}$ (unknown), will yield signals in the RGB channels, or **C.t** = **S**. We are almost there. We really need to get to the intensity vector in the succinct form: **A.I** =**S**. Hence, let us expand and reduce the elements of the signal component matrix: $t_k C_{jk} = I_k c_k \phi_k s_{jk}/i_k = I_k c_k \phi_k s_{jk}/(c_k w_k S_k) = I_k \phi_k s_{jk}/(w_k S_k)$. Hence, for the **A** matrix elements, we have $A_{jk} = s_{jk}\phi_k/(w_k S_k)$. Mostly, f_k will be unity. The **S** vector components are the measured signals in the RGB channels in the presence of the three discrete wavelengths: i.e., $S1 \equiv S_R$, $S2 \equiv S_G$, and $S3 \equiv S_B$ and $S_j = \sum_{k=1}^{3} A_{jk} I_k$.

4. Unfolding signals to intensities

The above was for a single three-color pixel (three individual CCD elements, or 4 with 2 combined). We now generalize to

encompass all pixels. Given a signal vector, $\mathbf{S}_{ij}$, for the (i,j) pixel and a corresponding matrix, $\underline{\mathbf{A}}_{ij}$, the intensity vector, $\mathbf{I}_{ij}$, is simply $\mathbf{I}_{ij} = (\underline{\mathbf{A}}_{ij})^{-1}\mathbf{S}_{ij} \equiv \underline{\mathbf{B}}_{ij}\mathbf{S}_{ij}$, where $\underline{\mathbf{A}}_{\boldsymbol{ij}}$ is the inverse matrix, an operation that is performed but once for each calibration exercise, giving an array of $\mathbf{B}_{ij}$ matrices.

Discrete λ	Source	Int filter	filter		Signal components	Channel
λ_1	I_1	$I_1 c_1 \phi_1$	t_1		$t_1 C_{11} t_2 C_{12} t_3 C_{13}$	R
λ_2	I_2	$I_2 c_2 \phi_2$	t_2	$\Rightarrow$	$t_1 C_{21} t_2 C_{22} t_3 C_{23}$	G
λ_3	I_3	$I_3 c_3 \phi_3$	t_3		$t_1 C_{31} t_2 C_{32} t_3 C_{33}$	B

5. Error propagation

Since the intensity vector components are obtained from linear operations on the signals, it is straightforward to look at the effects of errors on the signals in the RGB channels to errors on the discrete wavelengths intensities. Take, for example, a variance of σ_2 (G channel). We then have for the intensity component variances,

$$\begin{bmatrix} B_{12}\sigma_2 \\ B_{22}\sigma_2 \\ B_{32}\sigma_2 \end{bmatrix}.$$

Assuming Gaussian statistics for the three variances in $\mathbf{S}$, we get

$$\begin{bmatrix} (B_{11}^2\sigma_1^2 + B_{12}^2\sigma_2^2 + B_{13}^2\sigma_3^2)^{1/2} \\ (B_{21}^2\sigma_1^2 + B_{22}^2\sigma_2^2 + B_{23}^2\sigma_3^2)^{1/2} \\ (B_{31}^2\sigma_1^2 + B_{32}^2\sigma_2^2 + B_{33}^2\sigma_3^2)^{1/2} \end{bmatrix} \equiv (\underline{\mathbf{B}}^2.\sigma^2)^{1/2}$$

or, in general, for a pixel $(i,j) \equiv (\underline{B}_{ij}^2.\sigma_{ij}^2)^{1/2}$.

REFERENCES

[1] P. G. Carolan, A. Patel, N. J. Conway, R. J. Akers, C. A. Bunting, G. F. Counsell, J. Dowling, M. R. Dunstan, A. Kirk, F. Lott, M. N. Price, M. R. Tournianski, and M. J. Walsh, Rev. Sci. Instrum. **75**(10), 4069 (2004).

[2] A. R. Field, C. Michael, R. J. Akers, J. Candy, G. Colyer, W. Guttenfelder, Y.-c. Ghim, C. M. Roach, and S. Saarelma, and MAST Team, "Plasma rotation and transport in MAST spherical tokamak," Nucl. Fusion **51**, 063006 (2011).

[3] V. Rozhansky, E. Kaveeva, P. Molchanov, I. Veselova, S. Voskoboynikov, D. Coster, E. Fable, T. Puetterich, E. Viezzer, A. S. Kukushkin, and A. Kirk, "Understanding of impurity poloidal distribution in the edge pedestal by modelling," Nucl. Fusion **55**(7), 073017 (2015).

[4] T. Suzuki, R. j. Akers, D. A. Gates, S. Günter, W. W. Heidbrink, J. Hobirk, T. C. Luce, M. Murakami, J. M. Park, and M. Turnyanskiy, "Experimental investigation and validation of neutral beam current drive for ITER through ITPA Joint Experiments," Nucl. Fusion **51**, 083020 (2011).

[5] S. Shu, C. Xu, M. Chen, and Z. Yang, "Plasma image edge detection based on the visible camera in the EAST device," SpringerPlus **5**, 2050 (2016).

[6] A. Patel, P. G. Carolan, N. J. Conway, and R. J. Akers, "Z_{eff} profile measurements from bremsstrahlung imaging in the MAST spherical tokamak," Rev. Sci. Instrum. **75**(11), 4944 (2004).

[7] A. Patel, P. G. Carolan, N. J. Conway, C. A. Bunting, and R. J. Akers, "Versatile multiwavelength imaging diagnostic in the MAST spherical tokamak," Rev. Sci. Instrum. **75**(10), 4145 (2004).

[8] M. A. Van Zeeland, W. W. Heidbrink, J. H. Yu *et al.*, "Z_{eff} fast ion D_α imaging in the DIII-D tokamak," Plasma Phys. Control. Fusion **51**, 055001 (2009).

[9] M. P. S. Nightingale, G. W. Crawford, S. J. Gee, D. J. Hurford, D. Martin, M. R. Simmonds, R. T. C. Smith, C. C. Tsai, and S. E. V. Warder, "The MAST neutral beam injection system," Fusion Eng. Des. **56–57**, 529–532 (2001).

[10] R. J. Akers, L. C. Appel, and E. Arends, "On the neutral beam heating of MAST," in 18th Fusion Energy Conference. 4-10 October 2000, Sorrento, Italy, IAEA-CN-77, 2001.

[11] E. B. Bryce, "Color imaging array," US Patent 3,971,065 (20 July 1976).

[12] J. DiBella, M. Andreghetti, A. Enge, W. Chen, T. Stanka, and R. Kaser, "Improved sensitivity high-definition interline CCD using the kodak truesense color filter pattern," Proc. SPIE **7536**, 17–29 (2010).

[13] M. R. Gupta and T. Chen, "Vector color filter array demosaicing," Proc. SPIE **4306**, 374–382 (2001).

[14] S. Henderson, "Impurity transport studies on MAST," Ph.D. thesis, University of Strathclyde, 2014.

[15] J. McCone, "Impurity density and poloidal rotation measurements on MAST," Ph.D. thesis, University of Cork, 2011.

[16] E. Delabie, M. Brix, C. Giroud, R. J. E. Jaspers, O. Marchuk, M. G. O'Mullane, Y. Ralchenko, E. Surrey, M. G. Von Hellermann, K. D. Zastrow *et al.*, "Consistency of atomic data for the interpretation of beam emission spectra," Plasma Phys. Controlled Fusion **52**(12), 125008 (2010).

[17] S. S. Henderson, L. Garzotti, F. J. Casson, D. Dickinson, M. F. J. Fox, M. O'Mullane, A. Patel, C. M. Roach, H. P. Summers, M. Valovič, and MAST Team, "Neoclassical and gyrokinetic analysis of time-dependent helium transport experiments on MAST," Nucl. Fusion **54**(9), 093013 (2014).